GDCh

Research Article

Angewandte
Chemie
International Edition
www.angewandte.org

Unravelling the Crucial of Spatial Al Distribution to Realize Precise Alkali-Treatment for Target Acid-Catalyzed Reactions

Junjie Li[+], Huihui Chen[+], Wen Liu, Yuchun Zhi, Na Ta, Sujuan Xie, Longya Xu, Xiujie Li,* Xiangxue Zhu,* and Shutao Xu*

Abstract: Constructing mesoporous structure within zeolites by alkali-treatment is an effective protocol to improve their diffusion properties. However, undesirable changes in Brönsted acid site (BAS) densities always offset this advantage in acid-catalyzed reactions. In this context, the crucial roles of spatial aluminum (Al) distribution were unraveled during alkali-treatment of MFI zeolite and the desirable BAS density was achieved in obtained hierarchical samples for the target reactions. Various characterization methods, particularly the multiple one- and two-dimensional magic-angle spinning (MAS) NMR techniques, were performed to track the alkali-treatment processes. For the sample with a more uniform spatial Al distribution, more tetrahedral Al sites would fall off and migrate around the Si-OH in zeolite as $Al(OH)_4^-$. Those re-deposited $Al(OH)_4^-$ sites were easily transformed into NMR-invisible Al sites during the calcination process, which contributed negligibly to both Brönsted and Lewis acidities, thus being referred to "acid-free" Al species. While most tetrahedral Al sites were preserved after the alkali-treatment of sample with non-uniform Al distribution and the BAS density gradually increased with treatment time. According to the requirements of typical acid-catalyzed reactions, such as catalytic cracking of 1,3,5-triisopropylbenzene and methanol-to-olefins, the desired hierarchical zeolite catalysts were developed by matching the amounts of extracted Si and generated "acid-free" Al during the precise alkali-treatment.

[*] Dr. J. Li,[+] H. Chen,[+] Dr. W. Liu, Prof. Y. Zhi, Prof. N. Ta, Prof. S. Xie, Prof. L. Xu, Prof. X. Li, Prof. X. Zhu, Prof. S. Xu
The State Key Laboratory of Catalysis
Dalian Institute of Chemical Physics
Chinese Academy of Sciences, Dalian 116023 (P. R. China)
E-mail: xiujieli@dicp.ac.cn
    zhuxx@dicp.ac.cn
    xushutao@dicp.ac.cn

H. Chen[+]
University of Chinese Academy of Sciences, Beijing, 100049 (P. R. China)

H. Chen,[+] Prof. Y. Zhi, Prof. S. Xu
National Engineering Research Center of Lower-Carbon Catalysis Technology
Dalian Institute of Chemical Physics
Chinese Academy of Sciences, Dalian 116023 (P. R. China)
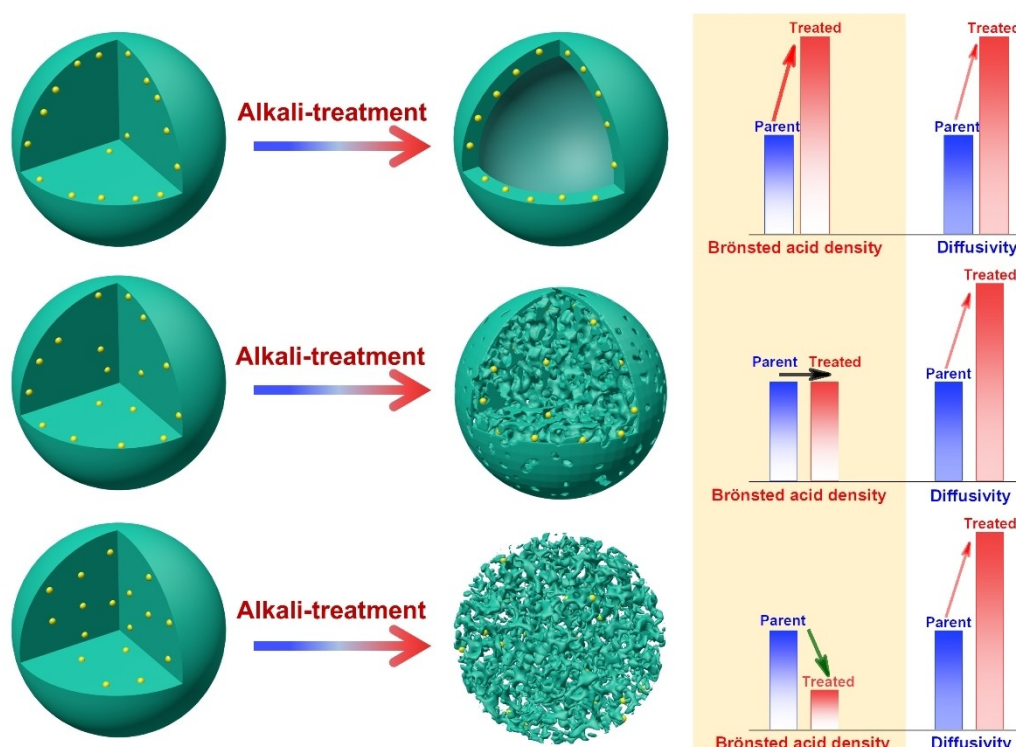
[+] These authors contributed equally to this work.

Introduction

Zeolites with mesopores or macropores have attracted much attention, benefitting from their stronger acidity, higher thermal stability, and better diffusion property.[1] Framework etching by alkali-treatment seems to be an ideal method to construct hierarchical structure within zeolites. This post-synthesis method offers a more straightforward scalability for application in industrial catalysis.[2] Significant porosity changes in MFI zeolites by NaOH treatment were first demonstrated in 2000 by Matsukata and co-workers.[3] Subsequent to this pioneering work, numerous works have reported the hierarchical zeolites prepared by desilication, and this technique has been successfully scaled up and widely applied in the development of heterogeneous catalysts for various reactions, including methanol to hydrocarbons, isomerization, alkylation, and cracking.[4]

However, the effect of the desilication process on acid properties has not received sufficient attention as that on hierarchical structures.[5] The desilication would afffect the acidity properties that play a significant role in acid-catalyzed reactions.[6] In general, alkali-treatment of zeolite leads to the decrease of bulk Si/Al ratio, and as a result, the acid amount is expected to increase.[2a] However, the actual situation is very complex. Table S1 lists the Brönsted acid site (BAS) densities or strong acid densities of pristine and alkali-treated MFI samples reported in literatures, unexpected variation trends of increase, constancy, or decrease can be found. Moreover, the reason for the distinct effects of desilication on acid densities variation in different samples remains undisclosed. Therefore, achieving desirable BAS densities in obtained hierarchical samples for the target reaction remains a great challenge.

In this work, three MFI samples with different spatial Al distributions were prepared and treated by NaOH. Their resultant hierarchical counterparts present distinguishable porosity features and BAS densities diverge largely (Figure 1). By tracking the structure and composition variation of zeolites during the alkali-treatment processes through high-angle angular dark-field (HAADF) scanning transmission electron microscopy (STEM), solid-state magic-angle spinning (MAS) NMR and elemental analysis techniques, we unraveled the crucial roles of spatial Al distribution in pristine zeolite in determining the removal degree of framework tetrahedral Al and modulating the acidity of hierarchical counterparts. Additionally, the variation rule of BAS densities in samples having different Al number per unit cell demonstrated this viewpoint. In this case, the

Figure 1. The distinct variation trends of porosity, Brönsted acid density, and diffusivity after alkali-treatment of MFI samples with different spatial Al distributions. The yellow dots denote framework Al atoms in zeolites.

precise alkali-treatment strategy of zeolites was proposed for achieving desirable BAS densities in their hierarchical counterparts, and the ideal catalysts for catalytic cracking of 1,3,5-triisopropylbenzene (1,3,5-TIPB) and methanol-to-olefins (MTO) reactions can be designed. acidity of hierarchical counterparts. Additionally, the variation rule of BAS densities in samples having different Al numbers per unit cell demonstrated this viewpoint. In this case, the precise alkali-treatment strategy of zeolites was proposed for achieving desirable BAS densities in their hierarchical counterparts, and the ideal catalysts for catalytic cracking of 1,3,5-TIPB and MTO reactions can be designed.

Results and Discussion

Improvement of Zeolite Diffusivity

HZ1-P and HZ2-P with distinct spatial Al distributions were synthesized using tetrapropylammonium hydroxide (TPAOH) and n-butylamine as the templates, respectively. The ultrathin section STEM-EDS images of HZ1-P in Figure 2a present an Al-rich shell, and the surface Si/Al ratio is much lower than the bulk Si/Al ratio (15.5 vs 34.4, Table 1). While HZ2-P displays a homogeneous Si–Al distribution in Figure 2b. Table 1 also presents a similar surface Si/Al ratio as that of the bulk (~32).

Then, HZ1-ATx and HZ2-ATx, treated by NaOH solution for x minutes ($x = 1$–30), were carefully prepared.

All the treated samples show typical MFI topology (Figure S1). The evolution of hierarchical structure was tracked by HAADF-STEM technique. The image of HZ1-P in Figure 2c exhibits few mesopores corresponding to the N_2 adsorption-desorption isotherm of type I in Figure S2. The appreciable mesopores started to appear in HZ1-AT1 with NaOH treated for 1 min as shown in Figure 2d, and then drastic etching, mainly localized in the central part of crystal, occurred at 3–15 min (Figure 2e–g). Finally, hollow-structured zeolite was formed after NaOH treating for 30 min (Figure 2h). All HZ1-ATx samples exhibit pronounced H2 hysteresis loops in Figure S2, demonstrating the formation of large pores with ink-bottle geometry.[7] The scanning electron microscope (SEM) images in Figure S3 show relatively integral external structure for HZ1-ATx samples, with a slight increase in the external surface for HZ1-AT30 (Table 1). Some mesopores were formed in HZ2-P after alkali-treatment (Figure S4), which distributed throughout the whole particles (Figure 2i–n). The HAADF-STEM and N_2 adsorption results illustrate that more mesopores with larger pore sizes were generated after a longer treatment time. HZ2-AT30 possessed a much higher mesopore volume of 0.468 cm³/g than that of HZ2-AT1 (0.236 cm³/g). Generally, regional or homogeneous etching happened on particles with different spatial Al distributions.

Intelligent gravimetric analyzer (IGA) was performed to characterize the diffusion properties of different samples. Toluene with a close kinetic diameter as the micropore sizes of MFI zeolite was used as the probe molecule to obtain
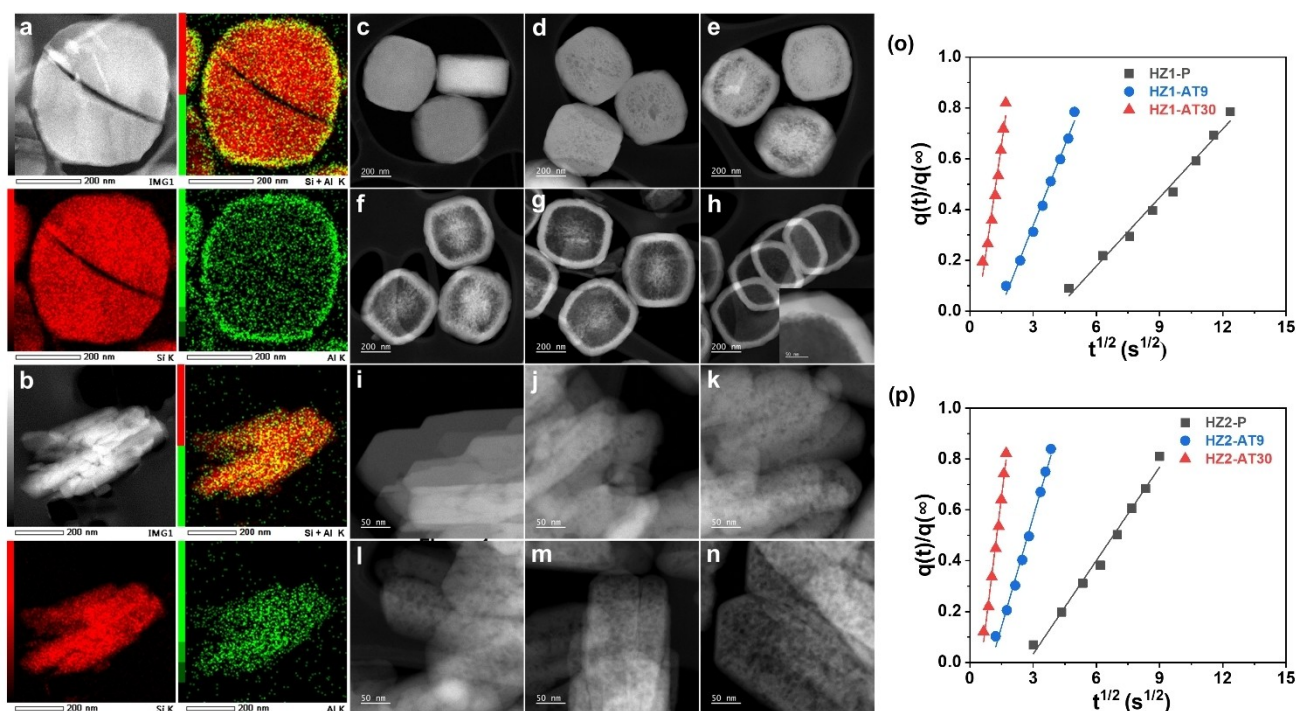
Figure 2. The ultrathin section STEM-EDS images of HZ1-P (a) and HZ2-P (b); HAADF-STEM images of HZ1-P (c), HZ1-AT1 (d), HZ1-AT3 (e), HZ1-AT9 (f), HZ1-AT15 (g), HZ1-AT30 (h), HZ2-P (i), HZ2-AT1 (j), HZ2-AT3 (k), HZ2-AT9 (l), HZ2-AT15 (m), HZ2-AT30 (n); adsorption rates of toluene in HZ1-P and HZ1-ATx (o), HZ2-P and HZ2-ATx (p) calculated by the IGA technique.

Table 1: The Si/Al ratios, N_2 adsorption results, and the amount of various OH groups in different ZSM-5 samples.

Samples	Bulk Si/Al ratio[a]	Surface Si/Al ratio[b]	Framework Si/Al ratio[c]	Physisorption results					^{1}H MAS NMR results[h] (mmol/g)		
				S_{BET}[d] (m^2/g)	S_{Ext}[e] (m^2/g)	V_{Micro}[e] (cm^3/g)	V_{Meso}[f] (cm^3/g)	V_{Total}[g] (cm^3/g)	Brönsted acid amount	Si—OH amount	Al—OH amount
HZ1-P	34.4	15.5	61.2	403	79	0.146	0.084	0.230	0.24	0.58	0.11
HZ1-AT1	31.1	–	52.7	413	67	0.153	0.116	0.269	0.30	0.17	0.05
HZ1-AT9	22.2	16.0	39.7	407	103	0.138	0.237	0.375	0.39	0.23	0.09
HZ1-AT30	15.3	15.2	31.0	413	112	0.134	0.248	0.382	0.54	0.21	0.09
HZ2-P	32.4	32.8	37.2	422	82	0.150	0.174	0.324	0.45	0.19	0.08
HZ2-AT1	30.1	–	51.7	424	106	0.139	0.236	0.375	0.30	0.18	0.07
HZ2-AT9	27.7	19.8	61.8	433	120	0.137	0.282	0.419	0.25	0.23	0.09
HZ2-AT30	22.5	17.3	83.7	460	183	0.123	0.468	0.591	0.18	0.40	0.12
HZ2-AT30-AW	34.8	34.6	82.3	462	179	0.123	0.417	0.540	0.18	0.33	0.09
HZ3-P	35.3	19.0	39.1	405	79	0.142	0.091	0.233	0.40	0.15	0.03
HZ3-AT30	25.5	15.0	37.7	461	177	0.122	0.302	0.424	0.41	0.39	0.07
HZ4-P	65.9	66.3	66.6	413	72	0.148	0.109	0.257	0.20	0.46	0.04
HZ4-AT30	38.7	–	65.7	427	146	0.120	0.358	0.478	0.21	0.22	0.06
HZ5-P	100.2	100.0	100.7	393	68	0.142	0.089	0.231	0.15	0.83	0.05
HZ5-AT30	55.8	–	75.9	393	111	0.131	0.274	0.405	0.18	0.21	0.03
HZ6-P	146.6	149.0	148.1	397	72	0.144	0.101	0.245	0.11	0.62	0.04
HZ6-AT30	88.0	–	98.3	402	163	0.111	0.247	0.358	0.16	0.18	0.04
HZ7-P	67.6	22.7	67.2	415	88	0.147	0.118	0.265	0.20	0.41	0.04
HZ7-AT30	32.2	–	52.2	441	137	0.128	0.342	0.470	0.30	0.25	0.07

[a] Determined by X-ray fluorescence (XRF) results (the Si/Al ratios of HZ7-P and HZ7-AT30 were determined by inductively coupled plasma optical emission spectrometer (ICP-OES)); [b] calculated by X-ray photoelectron spectroscopy (XPS) results (the Si/Al ratios of HZ4-P, HZ5-P, and HZ6-P were obtained by SEM-EDS results due to the limitation of XPS techinique for measuring samples with low Al content-high Si/Al ratio); [c] obtained by ^{29}Si MAS NMR results; [d] calculated by BET method; [e] calculated by t-plot method; [f] calculated by V_{Total}-V_{Micro}; [g] obtained at P/P_0 = 0.99; [h] acquired by ^{1}H MAS NMR results.

diffusivities of different samples based on Fick's second law. A good linear relationship between q(t)/q(∞) and $t^{1/2}$ for all samples is shown in Figure 2o and 2p. The diffusion time constant (D_{eff}/L^2), deduced from the slope, increased with a longer NaOH treatment time for both HZ1-P and HZ2-P as incremental mesopores or macropores were introduced, as presented by N_2 physisorption and HAADF-STEM results.

Distinct Effects on Zeolite Acidity

The bulk Si/Al ratios of the two kinds of samples obviously decreased after alkali-treatment for 1–30 min (Table 1). During the alkali-treatment process for both samples, the Al content in the filtrate was below 6 mg/L after alkali-treatment for 1–30 min (Figure S5), whereas the Si content was higher than 6000 mg/L after 30 min of treatment. Thus, alkali-treated samples presented lower Si/Al ratios compared with parent samples. However, the completely opposite variation trends of acid amount were observed for the treated HZ1-ATx and HZ2-ATx from ammonia temperature programmed desorption (NH₃-TPD) profiles in Figure 3a and 3b. The strong acid amount of HZ1-ATx increased by alkali-treatment for a longer time, while the case for HZ2-ATx was the opposite. HZ2-AT30 exhibits much lower strong acid sites compared with HZ2-P even though it has a lower bulk Si/Al ratio of 22.5. The framework Si/Al ratios of different samples were determined by ²⁹Si MAS NMR spectra (Figure S6, Table 1). As for HZ1-P

and HZ1-ATx, their framework and bulk Si/Al ratios synchronously decreased with the increase of treatment time (Figure 3c). While the opposite variation trends for the framework and bulk Si/Al ratios can be found for HZ2-P and HZ2-ATx (Figure 3d).

The variation trends in the quantity of BAS among different samples were further elucidated by analyzing ¹H MAS NMR spectra (Figure 4a and 4b). The signals at 1.6 and 2.0 ppm can be assigned to the isolated silanol groups (Si–OH) and geminal or vicinal Si–OH groups, respectively, while the signal at 2.6 ppm belongs to the aluminium hydroxyl (Al–OH) species. For samples with a relatively low Si/Al ratio, the peaks at 3.8 and 4.5 ppm are associated with two kinds of bridged hydroxyl species (Si(OH)Al), corresponding to the free BAS (I), and the hydrogen-bonded BAS (II), respectively.[8] Recently, Koller et al. also assigned the broader signal at 6 ppm to hydrogen-bonded Si-OH defects.[9] In order to verify these assignments, the ¹H–²⁷Al transfer of population in double-resonance (TRAPDOR) effect on the ¹H NMR intensities (Figure S7) and ¹H MAS NMR spectra of Na⁺ re-exchanged samples were performed (Figure S8). Under ²⁷Al irradiation, the signals of protons that are strongly coupled to Al atoms will be significantly suppressed, whereas those signals coupled with silicon atoms will remain unaffected. Thus, the signals at 2.6 ppm can be attributed to Al–OH species and the signals at 4.5 and 3.8 ppm can be attributed to BAS on basis of ¹H–²⁷Al TRAPDOR MAS NMR experiment for HZ1-P, HZ1-AT30, HZ2-P and HZ2-AT30.[10] The quantitative analysis of ¹H
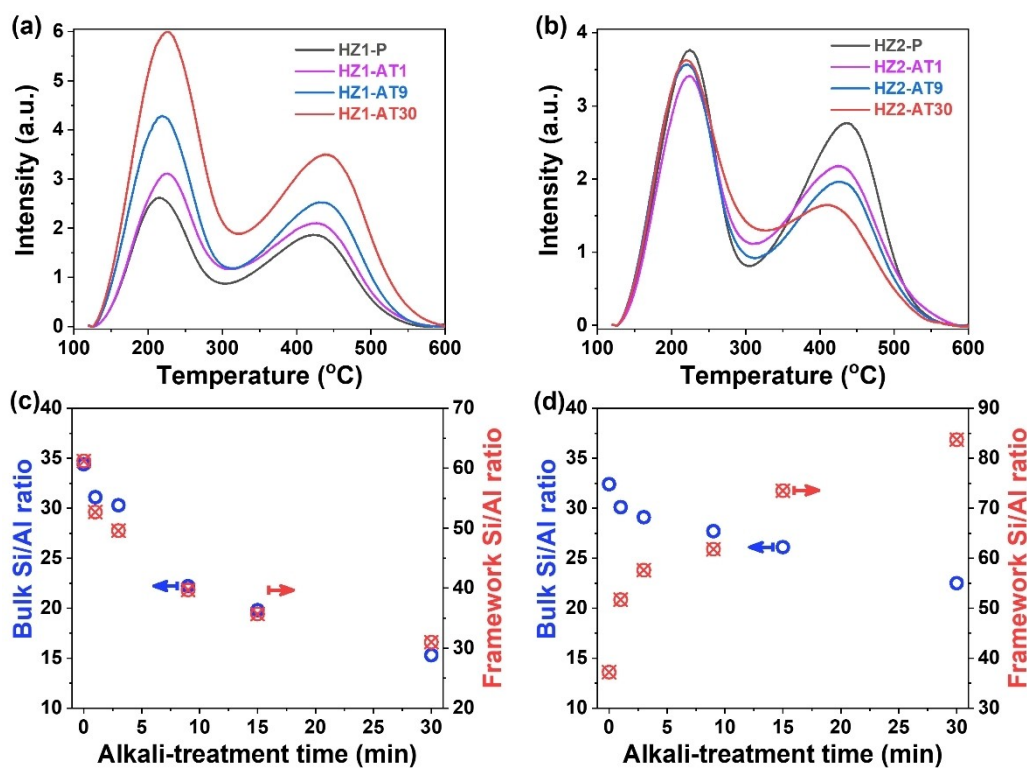

Figure 3. NH₃-TPD profiles of HZ1-P and HZ1-ATx (a), HZ2-P and HZ2-ATx (b); the comparison of bulk and framework Si/Al ratios of treated HZ1-ATx (c) and HZ2-ATx (d).
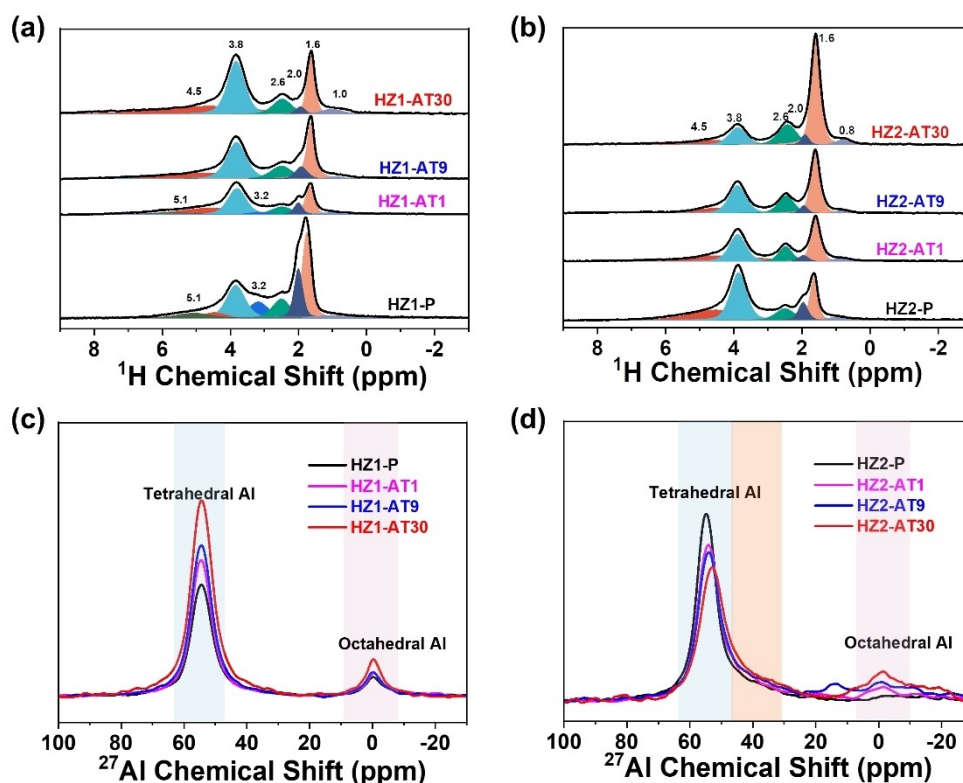
Figure 4. ^{1}H MAS NMR spectra of parent HZ1-P and alkali-treated HZ1-ATx (a), HZ2-P and alkali-treated HZ2-ATx (b); ^{27}Al MAS NMR spectra of parent HZ1-P and alkali-treated HZ1-ATx (c), HZ2-P and alkali-treated HZ2-ATx (d).

MAS NMR spectra reveals that the intensity of the peaks at 4.5 and 3.8 ppm exhibits an increasing trend with a longer treatment time for HZ1-ATx. Specifically, the amount of BAS increased from the initial value of 0.24 mmol/g to 0.54 mmol/g after 30 minutes treatment (Table 1, HZ1-P vs HZ1-AT30). However, the intensity of the two peaks decreased with a longer treatment time for HZ2-ATx, and the BAS amount decreased from 0.45 mmol/g for HZ2-P to 0.18 mmol/g for HZ2-AT30. The distinct trends in BAS variations during alkali- treatment may be associated with the coordination environment changes of tetrahedral Al species.

^{27}Al MAS NMR spectra were used to characterize the Al coordinations before and after NaOH treatment. The ^{27}Al MAS NMR spectra in Figure 4c show that most of Al sites (~90 %) are located in the framework coordinated by four Si–O species (55 ppm region) in HZ1-P and HZ1-ATx, and the proportions of octahedral Al sites (0 ppm region) remained almost unchanged after alkali-treatment except for HZ1-AT30 with a slight increase. HZ2-P has few octahedral Al sites (Figure 4d), while the percentage of octahedral Al sites slightly increases in alkali-treated HZ2-ATx. Simultaneously, the intensity of the peak belonging to tetrahedral Al sites decreases for HZ2-ATx and a broad shoulder resonance extending to the higher fields is observed, suggesting the possible generation of distorted tetrahedral Al sites (40–50 ppm region).[11] Combined with the ^{27}Al Multiple Quantum (MQ) MAS NMR spectra of HZ2-P and HZ2-AT30 in Figure S9, we can verify the

formation of some distorted tetrahedral Al sites in HZ2-AT30. The proportion of extra-framework Al sites including octahedral and distorted tetrahedral Al sites in HZ2-AT30 was ~20 % determined by the ^{27}Al MAS NMR spectrum, while the ratio of extra-framework Al sites in the HZ2-AT30 was determined to be ~75 % through the combined ^{1}H MAS NMR (BAS amount, 0.18 mmol/g) and XRF (Al content, 0.71 mmol/g) analysis. Although there may be some deviations among different quantitative methods, such a large difference can still indicate that there are some "non-Brönsted acid" Al species in the treated HZ2-ATx, which can not be detected by ^{27}Al MAS NMR because of their larger quadrupole coupling constant (QCC). XPS and XRF results (Table 1) illustrate that the surface Si/Al ratios are much lower than bulk Si/Al ratios in HZ2-AT9 and HZ2-AT30, and after a mild acid washing (HZ2-AT30-AW), the surface Si/Al ratio of HZ2-AT30 increased from 17.3 to 34.6 that is similar to its bulk Si/Al ratio. This corroborated the deposition of some Al sites onto the external surface of zeolite.

The nature of those re-deposited Al sites was deeply studied. As shown in Figure 5a, the ^{27}Al MAS NMR spectra of the alkali-treated Na-type sample NaZ2-AT30 and the NH$_4^+$ exchanged sample NH$_4$Z2-AT30 present a single peak at 55 ppm. Therefore, those re-deposited non-framework Al sites have a tetrahedral structure before high-temperature treatment. The spectrum of HZ2-AT30, obtained after calcination of the NH$_4$Z2-AT30 precursor, presents a significant reduction in peak intensity at 55 ppm. This
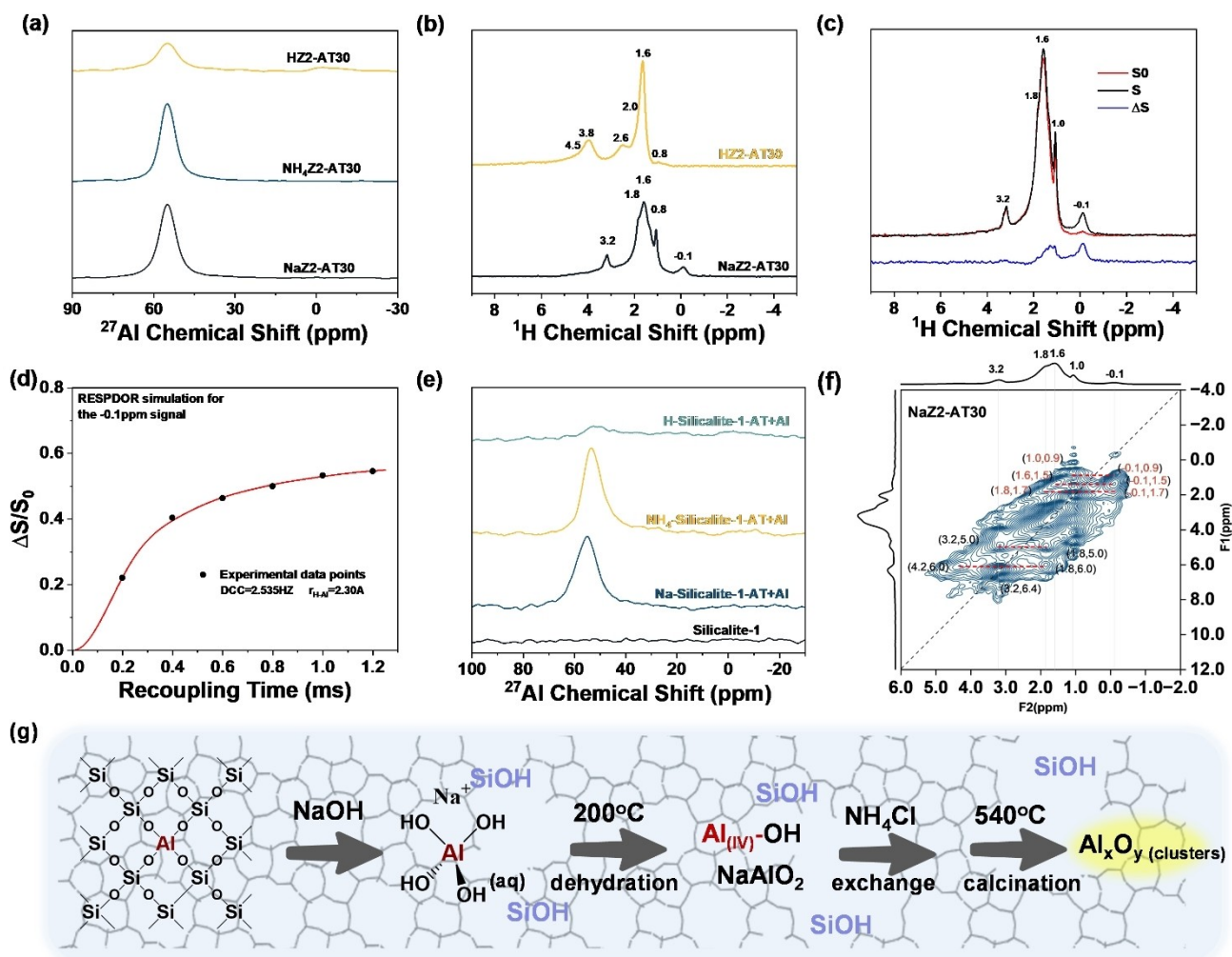
Figure 5. (a) ^{27}Al MAS NMR spectra of Na-type NaZ2-AT30, NH$_4$-type NH$_4$Z2-AT30, and HZ2-AT30; (b) ^{1}H MAS NMR spectra of HZ2-AT30 and NaZ2-AT30 dehydrated at 200°C; (c) ^{1}H–^{27}Al TRAPDOR MAS NMR spectra of NaZ2-AT30; (d) ^{1}H–^{27}Al S-RESPDOR simulation for the −0.1 ppm signal in ^{1}H MAS NMR spectrum of NaZ2-AT30; (e) ^{27}Al MAS NMR spectra of NaOH-treated Silicalite-1 (Na-type Na-Silicalite-1-AT+Al), ammonium-exchanged Na-Silicalite-1-AT+Al (NH$_4$-type NH$_4$-Silicalite-1-AT+Al), and calcined NH$_4$-Silicalite-1-AT+Al (H-type H-Silicalite-1-AT+Al); (f) ^{1}H-^{1}H DQ MAS NMR spectrum of NaZ2-AT30; (g) schematic diagram of the transformation of some framework Al sites during the alkali-treatment process.

indicates that some tetrahedral Al sites were transformed into NMR-invisible Al species during the high-temperature treatment process, which can be attributed to their larger QCC. By comparing the ^{1}H MAS NMR spectra of HZ2-AT30 and NaZ2-AT30 (Figure 5b), we can observe some ^{1}H NMR signals disappear after high-temperature calcination, which may correlate with the changes of ^{27}Al signals. The ^{1}H–^{27}Al TRAPDOR MAS NMR spectrum of NaZ2-AT30 (Figure 5c) demonstrates that only the ^{1}H NMR signal at −0.1 ppm is associated with Al, which disappears after the high-temperature calcination process, meanwhile the tetrahedral Al species may be transformed into some NMR-invisible Al species. It is possibly due to the condensation of Al–OH at elevated temperatures. The ^{1}H–^{27}Al symmetry-based rotational-echo saturation-pulse double-resonance (S-RESPDOR) method was adopted to explore the structure at −0.1 ppm. The fitted ^{1}H–^{27}Al distance (d(H–Al)) of the signal at −0.1 ppm ppm is 2.3 Å (Figure 5d), which is similar

to the d(H–Al) (~2.35 Å) of Al$_{IV}$–OH on the surface of Al$_2$O$_3$ (−0.2 ppm signal in the ^{1}H MAS NMR spectrum) in the previous work.[12] We also did Al deposition experiment with additional Al source (Al(NO$_3$)$_3$·9H$_2$O) during the NaOH treatment of pure-silica MFI (Silicalite-1), since Al(OH)$_4^-$ can stably exist in NaOH solution, Al-(NO$_3$)$_3$·9H$_2$O may deposit as Al(OH)$_4^-$ on Silicalite-1 in NaOH solution. The ^{27}Al MAS NMR spectrum of obtained Na-type Na-Silicalite-1-AT+Al shows that the peak for the deposited Al species overlaps with the signal of Al species in NaZ2-AT30 (Figure 5e). Furthermore, the peak intensity at 55 ppm in the ^{27}Al MAS NMR spectra of both the calcined H-Silicalite-1-AT+Al and HZ2-AT30 significantly decreased. Considering that NaAlO$_2$ exists as Al(OH)$_4^-$ species in aqueous solution, the dried powder NaAlO$_2$ was characterized by ^{1}H MAS NMR technique after dehydration and the obtained spectrum in Figure S10 presents an obvious signal at −0.1 ppm, indicating that Al(OH)$_4^-$ species can be

converted into $NaAlO_2$ rich in Al_{IV}-OH structures during the drying process. By ^1H–^1H Double Quantum (DQ) MAS NMR experiment of NaZ2-AT30 (Figure 5f), we found that those Al_{IV}–OH sites were closed to the Si-OH sites at 1.8, 1.6, and 0.8 ppm (the distance is smaller than 5 Å). Therefore, we can infer that those extracted Al sites redeposit around Si-OH groups. Figure 5g illustrates the transformation of some framework Al sites during the alkaline treatment process. Firstly, the framework Al on the zeolite was transformed into re-deposited $Al(OH)_4^-$ in the NaOH solution. Subsequently, those $Al(OH)_4^-$ sites transformed into into $NaAlO_2$ species rich in Al_{IV}-OH defects after drying. After ammonium ion-exchange and sequential calcination at 540 °C, those re-deposited Al species were converted into some NMR-invisible Al species (Al_xO_y clusters) because of their larger QCC. The ^1H MAS NMR and ^1H–^{27}Al TRAPDOR MAS NMR spectra of H-Silicalite-1-AT+Al presents few BAS (Figure S11), demonstrating the "non-Brönsted" property of those re-deposited Al sites.

The pyridine adsorption fourier transform infrared spectroscopy (Py-IR) spectra of HZ2-P and HZ2-AT30 were shown in Figure S12. According to the peak area for bands at 1545 and 1450 cm^{-1} and the related extinction coefficients, the ratio of Brönsted acid amount to Lewis acid amount (B/L ratio) was quantified. The B/L ratios of HZ2-P and HZ2-AT30 were 4.0 and 1.1. Combined with Py-IR and ^1H MAS NMR results, the Lewis acid amounts of HZ2-P and HZ2-AT30 can be calculated, which were 0.11 mmol/g and 0.16 mmol/g. Thus, it can be concluded that the Lewis acid amount increased by 0.05 mmol/g after alkali-treatment, however, the Brönsted acid amount decreased by ~0.50 mmol/g. The increased 0.05 mmol/g Lewis acid sites can be derived from the created Al-OH at 2.6 ppm which increased from 0.08 mmol/g to 0.12 mmol/g after alkali-treatment, the ^{27}Al MQ MAS NMR spectra of HZ2-P and HZ2-AT30 indicated the formation some six-coordinated and distorted tetrahedral Al sites that may contribute to the slight increase of Lewis acid amount. Generally, those re-deposited Al sites contributed negligibly to both BAS and LAS, which are "acid-free" sites.

Thus, it can be speculated that some Al sites in zeolite framework fell off when the surrounding structure (Si-(SiO)$_4$) were damaged during the alkali-treatment, meanwhile, those extracted Al species could rapidly deposit onto the created Si-OH groups and transformed to "acid-free" Al sites during the high-temperature dehydration process. In summary, most of the diminished BAS in HZ2-ATx were transformed into "acid-free" Al sites (re-deposited Al species).

Crucial Roles of Spatial Al Distribution

On the basis of previous TEM and elemental distribution results, we can deduce that the different spatial Al distributions may result in the opposite variation trends of BAS density for HZ1-ATx and HZ2-ATx. It seems likely that NaOH selectively removed the internal Si sites in HZ1-P that resulted in a hollow structure, and as a result, most of framework tetrahedral Al sites located at the outer-shell were preserved and the BAS density would increase due to the removal of more Si sites. For HZ2-P with uniformly distributed Al sites, the mesopores were homogeneously distributed throughout the crystals. Thus, the Al structure would be damaged when adjacent Si sites were removed, leading to a lower BAS density. Although the TEM results have provided the macroscopic morphological changes caused by alkali-treatment, the starting sites of desilication and the spatial distance information between newly generated hydroxyl species and BAS deserve further research.

The quantitative analysis of the ^1H MAS NMR spectra provides evidence that there was a preferential removal of silanol nests and silanol groups during alkaline treatment, as indicated by the significant decrease in the silanol content of the HZ1 sample after 1 minute of alkali-treatment (Table 1). Moreover, subsequent extraction of Si species resulted in the generation of new silanol groups, leading to a gradual increase in the silanol content after a longer alkali-treatment time. ^1H–^1H proton-driven spin diffusion (PDSD) MAS NMR spectra (Figure 6) can provide information on the proximity of different hydroxyl proton species during the alkali-treatment process. With a suitable mixing time, protons of different hydroxyl species that are close in space will show cross-peaks on the opposite diagonal of 2D NMR spectrum. In the 2D ^1H-^1H PDSD MAS NMR spectra of HZ1-P and HZ1-ATx with a mixing time of 500 ms, the absence of cross peaks between BAS protons and silanol protons is observed during the 30 minutes of alkali-treatment. That means the etching region, where the silicon hydroxyl groups generated, were distanced from the protons from tetrahedral Al sites, consequently most of tetrahedral Al sites were preserved after desilication and the BAS density greatly increased due to the removal of large numbers of Si sites. Although HZ2-P had fewer silanol groups compared with HZ1-P, it can be observed that there is spatial proximity between BAS and silanols in HZ2-P due to its uniform Al distribution (Figure 6). Moreover, the intensity of silanol groups involved in exchange with BAS increased in both HZ2-AT1 and HZ2-AT9. This indicates a progressive generation of new silanol groups being in spatial proximity to BAS. Thus, it can be concluded that the etching areas were close to the framework tetrahedral Al sites and more tetrahedral Al sites were damaged after a longer alkali-treatment time. Those damaged Al sites would fall off and deposit around the generated Si–OH when all surrounding Si sites were extracted. Meanwhile some extra-framework Al species would also be generated when a part of surrounding Si sites were leached out. For HZ2-AT30, the peak intensity of BAS involved in the exchange with silanol groups significantly decreased, which can be ascribed to the notable decrease in BAS density after 30 minutes treatment.

For further demonstration, three samples (HZ4-P, HZ5-P, and HZ6-P) with different Al numbers per unit cell (N_{Al}) of 1.45, 0.95 and 0.65 respectively were synthesized using a similar synthetic route as that of HZ2-P. Abundant mesorpores were created in alkali-treated (for 30 min) samples (Figure S13), which uniformly distributed throughout the crystals ascribed to the homogeneous spatial Al distribution
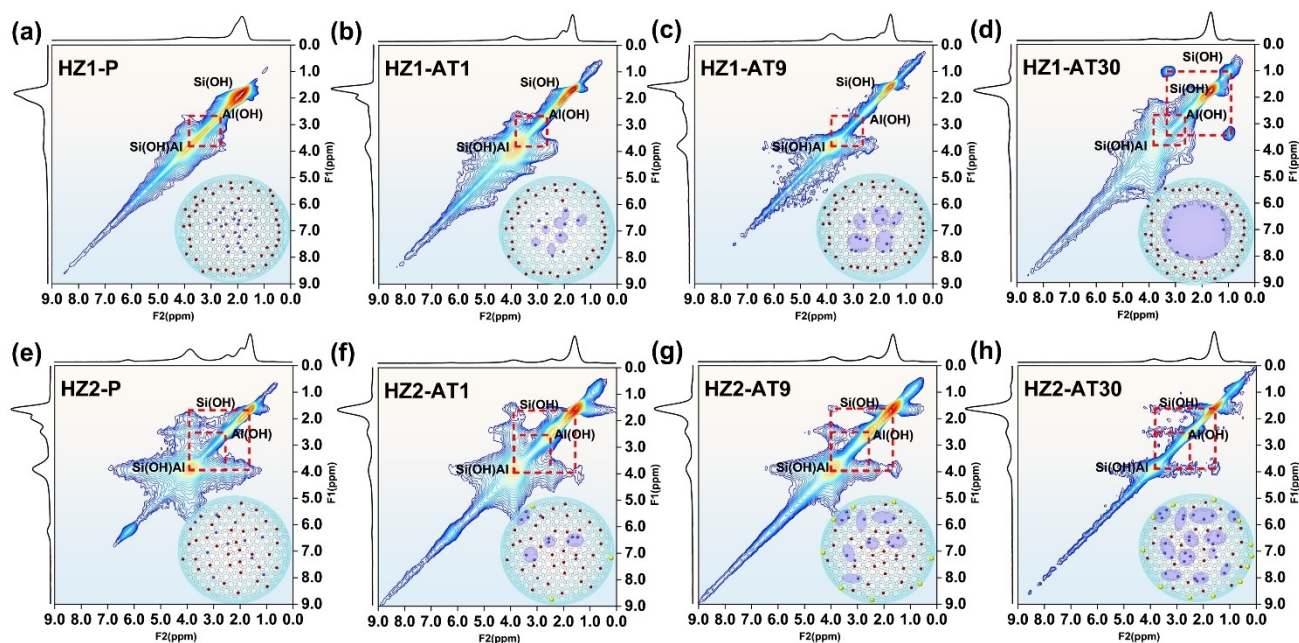
Figure 6. $^1H-^1H$ PDSD MAS NMR spectra of HZ1-P (a), HZ1-AT1 (b), HZ1-AT9 (c), HZ1-AT30 (d), HZ2-P (e), HZ2-AT1 (f), HZ2-AT9 (g), and HZ2-AT30 (h). The red, blue, or yellow dots denote framework Al atoms, silanol groups, or surface-deposited Al atoms in the inserted framework structures, respectively, and the blue circles represent created mesopores or macropores.

by elemental analysis (Table 1). ^1H MAS NMR spectra of pristine and alkali-treated samples are shown in Figure S14 and the quantitative analysis results are shown in Table 1. The ratios of BAS amount in alkali-treated samples to that in pristine samples ($BAS_{alkali-treated}/BAS_{pristine}$) were compiled in Figure 7. The $BAS_{alkali-treated}/BAS_{pristine}$ ratio decreased from 1.45 to 0.40 when the N_{Al} of the pristine sample increased from 0.65 to 2.87. The BAS density in HZ4-P having a N_{Al} of 1.45 kept almost unchanged after alikali-treatment (the $BAS_{alkali-treated}/BAS_{pristine}$ ratio was 1.05). Figure S15 presents the $^1H-^1H$ PDSD MAS NMR spectrum of HZ6-AT30, the cross peaks between BAS protons and silanol protons can be hardly observed. It can be deduced that the desilication zone was far from framework Al sites
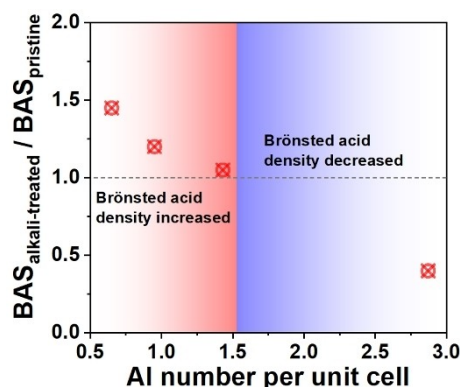
and more tetrahedral Al sites were preserved, and the BAS amount increased by 45% in HZ6-P ($N_{Al}=0.65$) through the alkali-treatment. Considering the heterogeneous Al distribution in HZ1-P ($N_{Al}=2.71$), there were some areas having a N_{Al} lower than 1.45 in the central part ascribed to the much larger N_{Al} (5.82) of outer-shell. As a result, the BAS amount of HZ1-ATx increased due to select removal of the inner part having the lower N_{Al}. Although HZ2-P possessed the similar N_{Al} with HZ1-P (2.87 vs 2.71), the BAS amount of HZ2-ATx decreased ascribed to the lack of some areas having a N_{Al} lower than 1.45.

Considering the existence of many extra-framework Al sites in HZ1-P that may influence the above conclusion, HZ7-P with similar bulk and framework Si/Al ratios was prepared by the similar synthesis route as HZ1-P. The ^{27}Al MAS NMR spectrum of HZ7-P (Figure S16) presents few extra-framework Al sites (at ~0 ppm). HZ4-P and HZ7-P presented similar framework Si/Al ratios but different spatial Al distributions (Table 1). As shown in Figure S13b and S13e, quite different hierarchical structures were constructed after alkali-treatment of the two samples. The TEM image of HZ4-AT30 (Figure S13b) presented uniform mesopores which centered at ~10 nm (Figure S17), while hollow particles with intact outer-shells can be observed in the TEM image of HZ7-AT30 (Figure S13e), corresponding to the H2 hysteresis loop found in the adsorption-desorption curve of HZ7-AT30 (Figure S17). Therefore, both the spatial Al distribution and Si/Al ratio play significant roles in constructing hierarchical structure in zeolites. Besides, the variation of Brönsted acid amount after alkali-treatment also differed a lot for HZ4-P and HZ7-P, which kept almost unchanged after alkali-treatment for HZ4-P (0.20 vs

Figure 7. The ratios of BAS amount of alkali-treated samples to that of pristine samples ($BAS_{alkali-treated}/BAS_{pristine}$) having different Al numbers per unit cell (N_{Al}).

Angew. Chem. Int. Ed. **2024**, e202416564 (8 of 11)

© 2024 Wiley-VCH GmbH

0.21 mmol/g, Table 1), while the changes of Brönsted acid amount increased by 50% after alkali-treatment for HZ7-P (Table 1 and Figure S16c). It follows that the changes of Brönsted acid amount between parent and alkali-treated samples closely correlated with the spatial Al distribution.

HZ3-P sample having a more uniform spatial Al distribution compared with HZ1-P (a larger surface Si/Al ratio, Table 1) was prepared by the seed-directed method using tetrapropylammonium bromide as the template, which also presented the non-spherical morphology and similar particle size as HZ2-P (Figure S18). 2D ^{1}H–^{1}H PDSD MAS NMR spectra (Figure S19) illustrate that the cross peaks between BAS protons and silanol protons can hardly be observed in HZ3-AT1, demonstrating that alkali-treatment indeed commences from the silicon-rich region and the removed Si sites in 1 min were far from BAS. While the cross peaks appeared after 30 min of treatment, indicating that the removed Si sites were gradually close to some tetrahedral Al sites and those Al sites would be damaged after a longer alkali-treatment. Figure S20 and Table 1 present similar BAS density for HZ3-P and HZ3-AT30. For HZ1-P having a more heterogeneous Al distribution compared with HZ3-P, those cross peaks between BAS protons and silanol protons can hardly be observed even after 30 min alkali-treatment and the BAS density greatly increased in HZ1-AT30. While those cross peaks can be found in 1 min alkali-treated HZ2-P having a uniform Al distribution, consequently the BAS density significantly

decreased in HZ2-AT30 obtained by a longer alkali-treatment time. In summary, the spatial Al distribution in zeolites determines the damage degree of framework tetrahedral Al sites and the amount of generated "acid-free" Al sites, finally influencing the BAS densities of alkali-treated samples. Considering the distinct spatial Al distribution for MFI zeolites prepared by different synthetic routes,[7,13] the BAS densities in alkali-treated samples may display distinct variation trends of increase, no change, or decrease (Table S1).

Accurate Alkali-Treatment to Prepare Desired Catalysts

Considering that both pore structure and acidity play significant roles in zeolite-catalyzed reactions,[14] the precise alkali-treatment method should be employed to acquire positively varied acidity. 1,3,5-TIPB serves as a model aromatic compound in the heavy oils, and its catalytic cracking into more valuable products (propylene, benzene, and cumene) is a very important process. Introducing additional mesopores or macropores into MFI zeolites, while maintaining the integrity of BAS, can remarkably enhance their catalytic activity.[15] For HZ1-P with a heterogeneous spatial Al distribution, the optimal alkali-treatment was 30 min benefited from incremental active sites (BAS density) and diffusivity (diffusion time constant) with a longer treatment time (Figure 8a).[16] HZ1-AT30 also
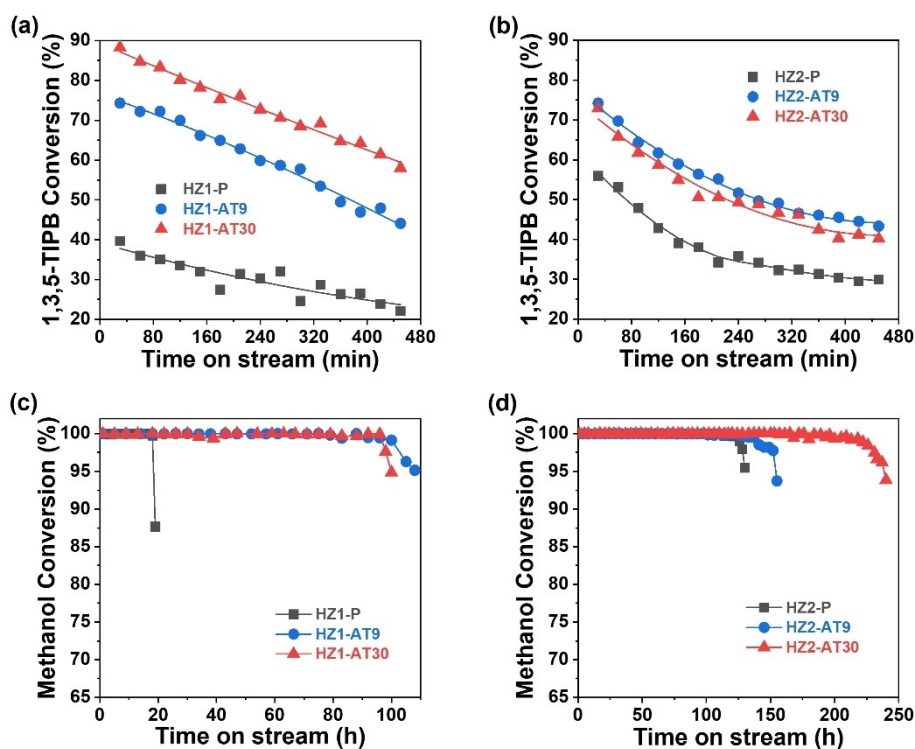

Figure 8. The 1,3,5-triisopropylbenzene (1,3,5-TIPB) conversions as a function TOS over HZ1-P and HZ1-ATx (a), HZ2-P and HZ2-ATx (b). Reaction conditions: 0.5 g catalyst, temperature of 350°C, WHSV of 4 h^{-1}, pressure of 0.1 MPa; the methanol conversions as a function of TOS over HZ1-P and HZ1-ATx (c), HZ2-P and HZ2-ATx (d). Reaction conditions: 0.5 g catalyst, temperature of 470°C, WHSV of 4 h^{-1}, pressure of 0.1 MPa, the methanol-water mixture molar ratio of 1:1.

Research Article

Angewandte
International Edition | Chemie

presented better catalytic performance compared with those ZSM-5 catalysts reported in literatures (Table S2). While the BAS density obviously decreased with prolonged alkali-treatment time for HZ2-P having a uniform spatial Al distribution, thus, HZ2-AT9 presented a slightly higher activity compared with HZ2-AT30 even though the diffusivity was greatly improved by extending alkali-treatment time (Figure 8b). Besides, the 1,3,5-TIPB cracking performance over HZ2-AT30-AW was compared with that over HZ2-AT30, as shown in Figure S21, HZ2-AT30-AW presented similar 1,3,5-TIPB conversions with HZ2-AT30 at different time on stream (TOS). Therefore, those "acid-free" Al sites contributed negligibly to the catalytic performance. HZ2-AT30 at different TOS. Therefore, those "acid-free" Al sites contributed negligibly to the catalytic performance.

Constructing hierarchical structure is also an effective method to improve the catalytic performance of MFI zeolite in MTH reactions.[17] However, an increase in BAS amount will result into a lower olefin selectivity and lower catalytic stability.[18] For HZ2-P with a uniform spatial Al distribution, the BAS density decreased with the increase of diffusivity from 1 min to 30 min of alkali-treatment, as anticipated, HZ2-AT30 displays the highest catalytic stability compared with HZ2-P and HZ2-AT9 (Figure 8d). The conversion efficiency ($g_{methanol}/g_{catalyst}$) over HZ2-AT30 was better than most hierarchical catalysts reported in recent literatures (Table S3). While HZ1-AT9 exhibits higher stability and olefins selectivity compared to HZ1-AT30 (Figure 8c, Figure S22), attributing to its relative lower BAS density that restricted the hydrogen transfer reactions and eventually coke deposition.[19] Although the catalytic stabilities were greatly enhanced over alkali-treated HZ1-ATx, they were still lower than those observed over HZ2-ATx due to the higher BAS densities in HZ1-ATx and their Al-rich shells and relative closed hierarchical structures.[4b] By analyzing the catalytic activity ($r(mmol_{[1,3,5-TIPB]} \cdot mmol_{[BAS]}^{-1} \cdot s^{-1})$) and conversion capacity ($g_{methanol}/g_{catalyst}$) as a function of diffusion time constant (D_{eff}/L^2, obtained by IGA curves) over different catalysts (Figure S23), it can be concluded that the optimal catalyst should take account of the changes of both BAS density and D_{eff}/L^2. Thus, the precise alkali-treatment of zeolites was proposed for targeted acid-catalyzed reactions, which can be realized by choosing the parent zeolite with suitable spatial Al distribution before treatment or modulating the amounts of extracted Si and created "acid-free" Al during treatment.

Conclusions

In this study, three MFI samples with comparable Si/Al ratios were synthesized and treated by NaOH, leading to the increased, unchanged, and decreased BAS densities in their hierarchical counterparts, respectively. By tracking the alkali-treatment processes through multiple NMR methods (including ^1H MAS NMR, ^{27}Al MAS NMR, ^{29}Si MAS NMR, and $^1H-^1H$ PDSD MAS NMR) and elemental analysis (XRF, ICP, and XPS) techniques, we demonstrate how

distinct spatial Al distribution resulted in distinct acidity variation. During the alkali-treatment of HZ2-P, a large number of tetrahedral Al sites fell off and migrated around the Si-OH in zeolite as $Al(OH)_4^-$. Those re-deposited $Al(OH)_4^-$ sites were transformed into NMR-invisible Al sites during the calcination process, which contributed negligibly to both Brönsted and Lewis acidities. For samples with similar spatial Al distribution but different N_{Al}, the $BAS_{alkali-treated}/BAS_{pristine}$ ratio was linearly increased and the BAS densities kept unchanged in the sample having a N_{Al} of 1.45 ($B_{alkali-treated}/B_{pristine} = 1.05$). Although the N_{Al} of HZ1-P was larger than 1.45 (2.71), there were some areas having a N_{Al} lower than 1.45 due to the heterogeneous Al distribution. As a result, most tetrahedral Al sites were preserved after alkali-treatment and the amount of BAS gradually increased with treatment time. For HZ2-P having a homogeneous Al distribution and a larger N_{Al} of 2.87, more tetrahedral Al sites were transformed to "acid-free" Al sites by prolonging alkali-treatment time that resulted in the gradually decreased BAS density. For HZ3-P having a more uniform spatial Al distribution compared with HZ1-P, the BAS amount kept unchanged after alkali-treatment.

In the context of different acid-catalyzed reactions, an accurate alkali-treatment of zeolites was proposed to acquire positively varied BAS amount in their hierarchical counterparts, which can be realized by choosing a parent zeolite with suitable spatial Al distribution or by matching the extraction degree of Si and Al sites during treatment (suitable treatment time). In the 1,3,5-TIPB cracking reactions, as expected, hierarchical HZ1-AT30 with largely preserved BAS presented the highest initial conversion. For MTO reactions, HZ2-AT30 demonstrated the longest lifetime of 240 h. This superior performance was mainly attributed to its largest diffusivity and lowest BAS density, which synergistically restricted the hydrogen transfer reactions and coke deposition. This work unraveled the crucial role of spatial Al distribution by determining the content of generated "acid-free" Al in alkali-treated MFI zeolite, which contributes to releasing the improvement space of alkali-treated MFI catalysts.

Conflict of Interest

The authors declare no conflict of interest.

Data Availability Statement

The data that support the findings of this study are available in the supplementary material of this article.

[1] a) L.-H. Chen, M.-H. Sun, Z. Wang, W. Yang, Z. Xie, B.-L. Su, *Chem. Rev.* **2020**, *120*, 11194–11294; b) D. P. Serrano, J. M. Escola, P. Pizarro, *Chem. Soc. Rev.* **2013**, *42*, 4004–4035; c) J. Pérez-Ramírez, C. H. Christensen, K. Egeblad, C. H. Christensen, J. C. Groen, *Chem. Soc. Rev.* **2008**, *37*, 2530–2542; d) K. Möller, T. Bein, *Chem. Soc. Rev.* **2013**, *42*, 3689–3707; e) Y. H. Liu, X. X. Wang, J. Y. Li, Q. Zhang, Z. J. Niu, S. Wang, Y. J. Gao, M. K. Gao, R. S. Bai, Y. D. Zhou, W. B. Fan, O. Terasaki, J. Xu, J. H. Yu, *Angew. Chem. Int. Ed.* **2023**, *62*, e202312131.

[2] a) D. Verboekend, J. Pérez-Ramírez, *Catal. Sci. Technol.* **2011**, *1*, 879–890; b) S. Mitchell, N.-L. Michels, K. Kunze, J. Pérez-Ramírez, *Nat. Chem.* **2012**, *4*, 825–831.

[3] M. Ogura, S.-y. Shinomiya, J. Tateno, Y. Nara, E. Kikuchi, M. Matsukata, *Chem. Lett.* **2000**, *29*, 882–883.

[4] a) Y. Jiao, L. Forster, S. Xu, H. Chen, J. Han, X. Liu, Y. Zhou, J. Liu, J. Zhang, J. Yu, C. D'Agostino, X. Fan, *Angew. Chem. Int. Ed.* **2020**, *59*, 19478–19486; b) J. Li, M. Liu, X. Guo, S. Xu, Y. Wei, Z. Liu, C. Song, *ACS Appl. Mater. Interfaces* **2017**, *9*, 26096–26106; c) J. Pastvova, D. Kaucky, J. Moravkova, J. Rathousky, S. Sklenak, M. Vorokhta, L. Brabec, R. Pilar, I. Jakubec, E. Tabor, P. Klein, P. Sazama, *ACS Catal.* **2017**, *7*, 5781–5795; d) B. Liu, W. Lu, Y. Liu, Q. Feng, Y. Huang, J. Shang, Y. Zhu, J. Dong, *AIChE J.* **2023**, *69*, e18201; e) M. Hartmann, A. G. Machoke, W. Schwieger, *Chem. Soc. Rev.* **2016**, *45*, 3313–3330; f) M. Moliner, C. Martínez, A. Corma, *Angew. Chem. Int. Ed.* **2015**, *54*, 3560–3579; g) K. A. Tarach, J. Martinez-Triguero, S. Valencia, K. Wojciechowska, F. Rey, K. Góra-Marek, *Appl. Catal. B* **2023**, *338*, 123066; h) Y. Song, B. Peng, R. Y. Wang, L. Han, W. H. Zhao, L. Wang, H. T. Song, W. Lin, *Chem. Eng. J.* **2023**, *476*, 146600.

[5] M. Milina, S. Mitchell, P. Crivelli, D. Cooke, J. Pérez-Ramírez, *Nat. Commun.* **2014**, *5*, 3922.

[6] a) S. Sartipi, K. Parashar, M. J. Valero-Romero, V. P. Santos, B. van der Linden, M. Makkee, F. Kapteijn, J. Gascon, *J. Catal.* **2013**, *305*, 179–190; b) K. Lee, S. Lee, Y. Jun, M. Choi, *J. Catal.* **2017**, *347*, 222–230; c) C. D. Lago, H. P. Decolatti, L. G. Tonutti, B. O. Dalla Costa, C. A. Querini, *J. Catal.* **2018**, *366*, 16–27; d) Y. Liao, R. Zhong, M. d'Halluin, D. Verboekend, B. F. Sels, *ACS Sustainable Chem. Eng.* **2020**, *8*, 8713–8722; e) Y. Yu, D. Zhang, N. Wei, K. Yang, H. Gong, C. Jin, W. Zhang, S. Huang, *J. Mol. Catal.* **2020**, *483*, 110768; f) Z. Wang, R. Zhang, J. Wang, Z. Yu, Y. Xiang, L. Kong, H. Liu, A. Ma, *Fuel* **2022**, *313*, 122669.

[7] J. C. Groen, T. Bach, U. Ziese, A. M. Paulaime-van Donk, K. P. de Jong, J. A. Moulijn, J. Pérez-Ramírez, *J. Am. Chem. Soc.* **2005**, *127*, 10792–10793.

[8] a) M. Hunger, S. Ernst, S. Steuernagel, J. Weitkamp, *Microporous Mater.* **1996**, *6*, 349–353; b) M. Hunger, *Catal. Rev.* **1997**, *39*, 345–393; c) W. Zhang, D. Ma, X. Liu, X. Liu, X. Bao, *Chem. Commun.* **1999**, 1091–1092.

[9] C. Schroeder, V. Siozios, M. Hunger, M. R. Hansen, H. Koller, *J. Phys. Chem. C* **2020**, *124*, 23380–23386.

[10] L. Chen, Q. Wang, B. Hu, O. Lafon, J. Trébosc, F. Deng, J.-P. Amoureux, *Phys. Chem. Chem. Phys.* **2010**, *12*, 9395–9405.

[11] a) K. Chen, S. Horstmeier, V. T. Nguyen, B. Wang, S. P. Crossley, T. Pham, Z. Gan, I. Hung, J. L. White, *J. Am. Chem. Soc.* **2020**, *142*, 7514–7523; b) J. Barras, J. Klinowski, D. W. McComb, *J. Chem. Soc. Faraday Trans.* **1994**, *90*, 3719–3723; c) B. Fan, D. Zhu, L. Wang, S. Xu, Y. Wei, Z. Liu, *Inorg. Chem. Front.* **2022**, *9*, 3609–3618.

[12] a) M. Taoufik, K. C. Szeto, N. Merle, I. D. Rosal, L. Maron, J. Trébosc, G. Tricot, R. M. Gauvin, L. Delevoye, *Chem. Eur. J.* **2014**, *20*, 4038–4046; b) Q. Wang, W. Li, I. Hung, F. Mentink-Vigier, X. Wang, G. Qi, X. Wang, Z. Gan, J. Xu, F. Deng, *Nat. Commun.* **2020**, *11*, 3620.

[13] a) T. T. Le, W. Qin, A. Agarwal, N. Nikolopoulos, D. Fu, M. D. Patton, C. Weiland, S. R. Bare, J. C. Palmer, B. M. Weckhuysen, J. D. Rimer, *Nat. Catal.* **2023**, *6*, 254–265; b) J. C. Groen, W. Zhu, S. Brouwer, S. J. Huynink, F. Kapteijn, J. A. Moulijn, J. Pérez-Ramírez, *J. Am. Chem. Soc.* **2007**, *129*, 355–360; c) H. Shen, M. Liu, J. Li, X. Li, S. Xie, F. Chen, L. Xu, X. Guo, C. Song, X. Zhu, *Ind. Eng. Chem. Res.* **2021**, *60*, 9098–9106; d) F. Jiao, P. Y. Yu, Y. C. Cui, H. Li, Q. Hu, Y. A. Xu, S. Mintova, H. L. Guo, H. B. Du, *Angew. Chem. Int. Ed.* **2023**, *62*, e2023104.

[14] a) G. Busca, A. Gervasini, in *Advances in Catalysis, Vol 67, Vol. 67* (Ed.: C. Song) **2020**, pp. 1–90; b) Y. C. Chai, W. L. Dai, G. J. Wu, N. J. Guan, L. D. Li, *Acc. Chem. Res.* **2021**, *54*, 2894–2904; c) V. Van Speybroeck, K. Hemelsoet, L. Joos, M. Waroquier, R. G. Bell, C. R. A. Catlow, *Chem. Soc. Rev.* **2015**, *44*, 7044–7111.

[15] a) P. Kortunov, S. Vasenkov, J. Karger, R. Valiullin, P. Gottschalk, M. F. Elia, M. Perez, M. Stocker, B. Drescher, G. McElhiney, C. Berger, R. Glaser, J. Weitkamp, *J. Am. Chem. Soc.* **2005**, *127*, 13055–13059; b) Z. X. Qin, L. Hafiz, Y. F. Shen, S. Van Daele, P. Boullay, V. Ruaux, S. Mintova, J. P. Gilson, V. Valtchev, *J. Mater. Chem. A* **2020**, *8*, 3621–3631; c) M. Sun, S. Gao, Z. Hu, T. Barakat, Z. Liu, S. Yu, J. Lyu, Y. Li, S. Xu, L. Chen, B. Su, *Nat. Sci. Rev.* **2022**, *9*.

[16] a) V. Babic, L. X. Tang, Z. X. Qin, L. Hafiz, J. P. Gilson, V. Valtchev, *Adv. Mater. Interfaces* **2021**, *8*, 2000348; b) W. H. Cui, D. L. Zhu, J. Tan, N. Chen, D. Fan, J. Wang, J. F. Han, L. Y. Wang, P. Tian, Z. M. Liu, *Chin. J. Catal.* **2022**, *43*, 1945–1954.

[17] a) Q. M. Sun, Z. K. Xie, J. H. Yu, *Natl. Sci. Rev.* **2018**, *5*, 542–558; b) X. C. Zhu, J. P. Hofmann, B. Mezari, N. Kosinov, L. L. Wu, Q. Y. Qian, B. M. Weckhuysen, S. Asahina, J. Ruiz-Martinez, E. J. M. Hensen, *ACS Catal.* **2016**, *6*, 2163–2177; c) S. Lopez-Orozco, A. Inayat, A. Schwab, T. Selvam, W. Schwieger, *Adv. Mater.* **2011**, *23*, 2602–2615.

[18] a) M. Dyballa, P. Becker, D. Trefz, E. Klemm, A. Fischer, H. Jakob, M. Hunger, *Appl. Catal. A* **2016**, *510*, 233–243; b) M. Dyballa, U. Obenaus, M. Blum, W. L. Dai, *Catal. Sci. Technol.* **2018**, *8*, 4440–4449; c) J. J. Li, M. Liu, S. S. Li, X. W. Guo, C. S. Song, *Ind. Eng. Chem. Res.* **2019**, *58*, 1896–1905; d) J. Zhang, L. J. Xu, Y. F. Zhang, Z. H. Huang, X. M. Zhang, X. Z. Zhang, Y. Y. Yuan, L. Xu, *J. Catal.* **2018**, *368*, 248–260.

[19] a) D. Mores, J. Kornatowski, U. Olsbye, B. M. Weckhuysen, *Chem. Eur. J.* **2011**, *17*, 2874–2884; b) C. D. Chang, C. T. W. Chu, R. F. Socha, *J. Catal.* **1984**, *86*, 289–296.

Research Article

Zeolite Catalysis

J. Li, H. Chen, W. Liu, Y. Zhi, N. Ta, S. Xie, L. Xu, X. Li,* X. Zhu,* S. Xu* —————— **e202416564**

Unravelling the Crucial of Spatial Al Distribution to Realize Precise Alkali-Treatment for Target Acid-Catalyzed Reactions
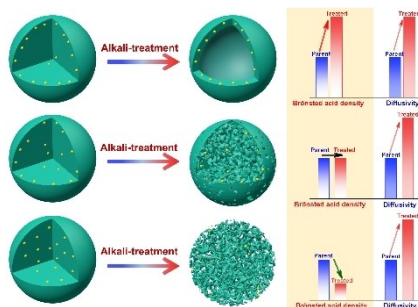
Undesirable changes (increase, no change, or decrease) in Brönsted acid densities were always illustrated in alkali-treated zeolites, which offset the advantage of improved diffusivity during acid-catalyzed reactions. In this context, the crucial roles of spatial aluminum distributions in the modulation of zeolite acidity were unraveled. Finally, a precise alkali-treatment of zeolites was proposed for better catalytic performance.